Journal Pre-proof

Spectroscopic study of volcanic ashes

Fabrizio Bardelli (Conceptualization) (Writing - original draft) (Writing - review and editing) (Formal analysis), Gabriele Giuli (Conceptualization) (Writing - original draft) (Writing - review and editing) (Formal analysis), Francesco Di Benedetto (Conceptualization) (Writing - original draft) (Writing - review and editing) (Formal analysis) (Investigation), Pilar Costagliola (Investigation), Giordano Montegrossi (Conceptualization) (Writing - original draft) (Writing - review and editing) (Investigation), Valentina Rimondi (Writing - review and editing), Maurizio Romanelli (Investigation), Luca A Pardi (Investigation), Germana Barone (Conceptualization) (Writing - original draft) (Writing - review and editing) (Resources), Paolo Mazzoleni (Conceptualization) (Writing - original draft) (Writing - review and editing) (Resources)

PII: S0304-3894(20)31202-4

DOI: https://doi.org/10.1016/j.jhazmat.2020.123213

Reference: HAZMAT 123213

To appear in: *Journal of Hazardous Materials*

Received Date: 17 January 2020

Revised Date: 11 June 2020

Accepted Date: 12 June 2020

Please cite this article as: Bardelli F, Giuli G, Di Benedetto F, Costagliola P, Montegrossi G, Rimondi V, Romanelli M, Pardi LA, Barone G, Mazzoleni P, Spectroscopic study of volcanic ashes, *Journal of Hazardous Materials* (2020), doi: https://doi.org/10.1016/j.jhazmat.2020.123213

Spectroscopic study of volcanic ashes

Bardelli Fabrizio[1], Giuli Gabriele[2], Di Benedetto Francesco[3], Costagliola Pilar[3], Montegrossi Giordano[4], Rimondi Valentina[3], Romanelli Maurizio[3], Pardi Luca A[5], Barone Germana[6], and Mazzoleni Paolo[6]

[1] CNR-Nanotec, c/o Department of Physics, La Sapienza University, Piazzale Aldo Moro, 5 – 00185 Roma

[2] School of Science and Technology-Geology div., University of Camerino, Via Gentile III da Varano – 62032 Camerino, Italy

[3] Department of Earth Sciences, University of Firenze, Via G. La Pira, 4 – 50121 Firenze, Italy

[4] CNR – Institute of Geosciences and Georesources, Via G. Moruzzi, 1 – 56124 Pisa, Italy

[5] CNR – Institute of Chemical-Physical Processes. Via G. Moruzzi, 1 – 56124 Pisa, Italy

[6] Department of Geological, Biological, and Environmental Sciences, University of Catania, Corso Italia 55 –95129 Catania, Italy

Graphical abstract

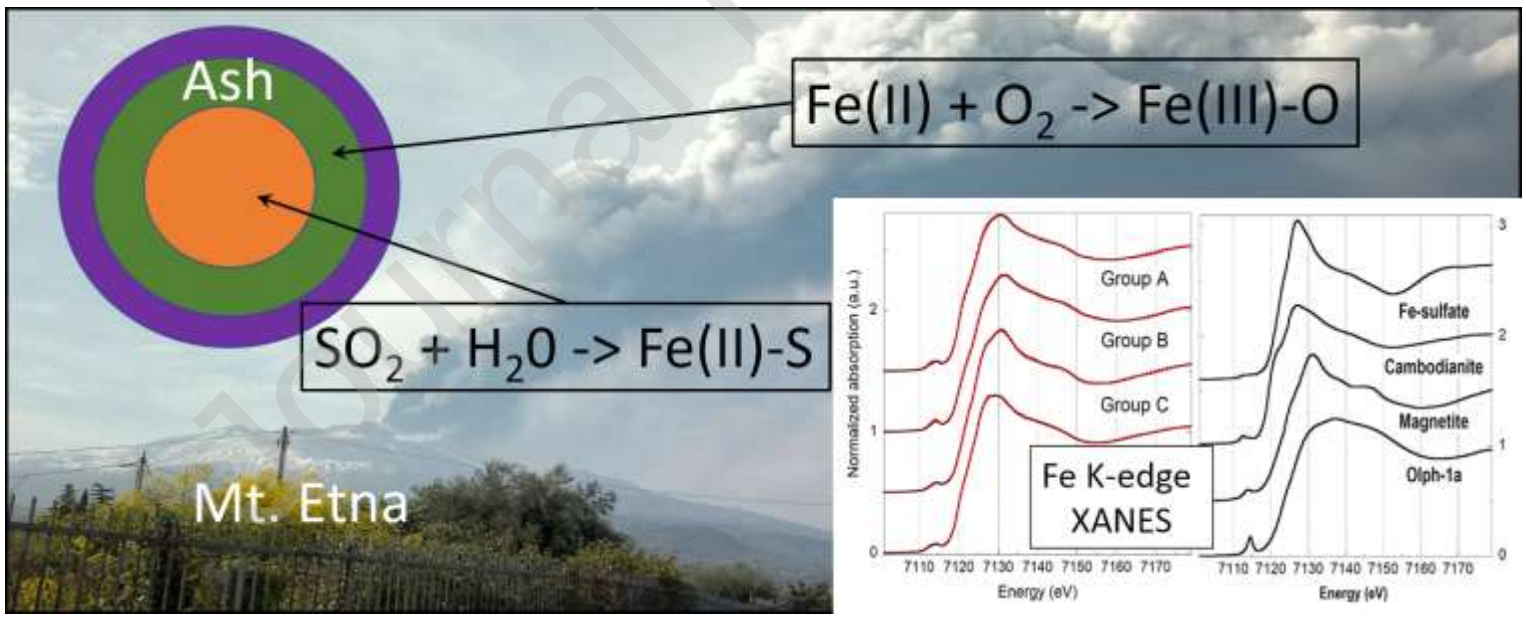

Highlights

- A complex mineralogical assemblage was revealed
- Fe(II) and Fe(III) species were detected in a variety of coordination environments
- The Fe oxidation state and speciation is not affected by water
- Significant changes were evidenced as a function of particle granulometry
- Ashes surface features may prevent direct exposure to mobile and toxic Fe(II)

Abstract

Volcanic ashes particles are subjected to substantial modification during explosive eruptions. The mineralogical and compositional changes have important consequences on the environment and human health. Nevertheless, the relationship between the speciation of iron (Fe) and the mineralogical composition and particle granulometry of the ashes, along with their interaction with water, are largely unknown. In particular, the Fe oxidation state and the possible formation of new Fe-bearing phases in presence of S, Cl, and F in the plume are key points to assess the impact of the ashes.

Fragmental material ejected during volcanic activity (tephra) in 2013, was collected on the Mt. Etna (Italy) and investigated using a multi-technique approach that included conventional Electron Paramagnetic Resonance (EPR), high field EPR (HFEPR), EchoEPR, and Fe K-edge X-ray Absorption Spectroscopy (XAS). These element-selective techniques allowed obtaining a detailed information on the oxidation state and coordination environment of Fe, and of its speciation in the ash samples as a function of the granulometry. A complex mineralogical assemblage, consisting of variable amounts of nanometric crystalline Fe inclusions in a glass matrix, and of Fe-oxides and Fe-sulfur phases was revealed. A risk assessment of the ashes is attempted.

Keywords: Volcanic ash, explosive eruption, granulometry, Iron speciation, XAS, EPR

1. Introduction

Volcanic ashes have received large attention in the recent years also because they are a major source of Fe release into the environment, which may lead to important adverse ecological [1] and toxicological [2] outcome. Fe speciation, in particular, can strongly influence the health impact of the ashes, determining the level of Fe solubility and, therefore, mobility in the environment [3]. Iron in volcanic ashes has been recently claimed to play a role in numerous environmental processes, even if its rate of dissolution from the glass at ambient conditions is generally low. For example, Fe and Al released by volcanic ash particles during weathering can form stable compounds with P_2O_5 [4] or stabilize soil organic carbon (SOC) in the typical black 1A horizon of Andosols, strongly influencing the soil fertility. Another important aspect of volcanic Fe is its role in marine ecosystems, such as, for example, micronutrient for the phytoplankton growth [1]. The analysis of the Fe released in hydric systems is also of interest, because toxic 3d transition metals such as V or Cr have an affine chemical behavior [5]. The knowledge of the possible presence of Fe-rich phases in volcanic ashes, and of the Fe oxidation state and coordination environment, is important to assess the Fe environmental impact. Volcanic ashes were also considered for industrial applications. In particular, the Fe-oxides contained in volcanic ashes have been used as catalysts to synthesize carbon nanotubes or nanofibers [6].

It has recently been proposed that the abundance of Fe in volcanic ash could be an health threat because it may induce hydroxyl radical generation on the surface of glassy particles through the Fenton reaction [2]:

$$Fe(II) + H_2O_2 \rightarrow Fe(III) + OH^- + HO\cdot$$

Mt. Etna is one of the most active volcanoes in the world, and in recent times, it has been characterized by frequent summit eruptive activity. In particular, starting from 2011, the New South East Crater (hereafter NSEC), one of the four summit craters of the volcano (Figure 1), produced 'episodic' eruption events, consisting of recurrent lava fountains, generally associated with lava flow emissions, lasting from a few weeks to months [7]. Episodic eruptions at NSEC occurred in 2011–12 (25 episodes between January 2011 and April 2012 [8] and 19 episodes between February and December 2013 [9]), and more recently (12 episodes between 2014 to 2018 [10–15]).

Although these paroxysmal events have shown different characteristics in terms of magnitude, duration, and eruptive styles [16], they were characterized by a common feature: they all produced an eruption plume associated with a tephra (i.e. solid material ejected during the volcanic activity) fallout event, which was recorded at different distances from the NSEC eruptive center. The occurrence of several lava fountains at NSEC in the period February to April 2013 allowed a sampling campaign of the fallout deposits formed during different paroxysms and distances from the NSEC. Recently, the mineralogical and geochemical surface modification of the same ash samples emitted by Mt. Etna during 2013 activity has been described at the nanoscale, highlighting the presence of nanometric magnesioferrite ($MgFe_2O_4$) and, for the first time, of dendrites of metallic iron [17].

In this work, a set of Mt. Etna ash samples, including those studied in the above-mentioned work [17], were sieved to obtain different grain size fractions with the aim to investigate if the Fe chemical and physical features are influenced by the amount of exposed particle surface. The effects of water on the Fe oxidation state was monitored on selected samples. A detailed characterization of the bulk Fe speciation was

obtained by means of a multi-technique approach that included X-ray Absorption Spectroscopy (XAS), Electron Paramagnetic Resonance (EPR), High Field Electron Paramagnetic Resonance (HFEPR), and Electron Spin Echo (ESE) spectroscopies.

2. Materials and methods

2.1 Materials

The studied ashes were emitted during different eruptions of the 2013 sequence, with the exception of the ET sample that belongs to an eruption event occurred in 2011 (Table 1). According to the recommendation of Stewart et al. (2013) [18], all volcanic ash samples were collected and stored immediately after the eruption to avoid contamination with other natural or anthropic dusts and with water. Aliquots of some of the samples (GIA, SVE, STE, FIA, BEL, ZAF) were used in a previous study that was focused on the chemical and mineralogical surface modifications occurring to the ashes during the eruption [17]. Considering the homogeneity of the Mt. Etna products emitted in the considered time range [19], we refer to the work of Barone et al. [17] for a detailed characterization of the grain size and other bulk properties.

Fractions with grain size greater and smaller than 850μm were obtained for each sample aliquot. When possible, fractions with grain size < 850 μm were sieved again to obtain a fraction with smaller particles (< 63μm). For the sample ET only, a larger set of granulometric classes was realized, including the raw, <1000, <500, <250, <125, <63μm fractions. Aliquots of the sieved fractions were leached by using ultrapure water for 30, 90, or 180minutes.

2.2 Methods

2.2.1 Paramagnetic Resonance spectroscopies

Conventional continuous wave (cw) EPR and pulsed ESE spectroscopic investigations were performed on loose ash samples wrapped in Teflon bags and inserted into amorphous silica tubes. Data were first acquired at room temperature (RT) for identification of paramagnetic centers by using a Bruker ER 200D-SRC spectrometer operating at X-Band (~9.5GHz). The operating frequency value was calibrated by using DPPH radical [*2,2-di(4-tert-octyl-phenyl)-1-picrylhydrazyl*, g = 2.0037] as external standard. Cw-EPR measurements were carried out also at 35 K, to improve the spectral quality and to perform the spectral attribution of the radical species, by using a Bruker ELEXYS X-band EPR, equipped with an Oxford CF935 cryostat and a dielectric cavity with high Quality (Q) factor.

Additional high field/high frequency (~190GHz) EPR measurements were carried out on selected samples at room temperature by using a HFEPR spectrometer, in single-pass mode. The source consists of a Gunn Effect diode emitting at 95 GHz (W band) equipped with a doubler to produce a 190GHz radiation. The magnet is a superconducting magnet (Oxford Instruments) operating at a maximum field of 12T. The detector is a hot electron bolometer (QMC Instruments). A modulation amplitude of 0.01mT and 5.3 kHz modulation frequency were appropriate values to observe reproducible spectra. Spectra were acquired at a scan speed of 1mT per minute. Pressed pellets of the powders

mixed with KBr were prepared to control the interactions of the crystallite with the intense external magnetic fields.

Pulsed ESE investigations were aimed to the acquisition of field swept Echo-EPR. All measurements were carried out at X-band and at 35 K on the same Bruker ELEXYS X-band EPR mentioned before. Spectra were acquired after a two-pulse π/2-τ-π-τ sequence at operating frequency of ~9.70 GHz. Magnetic field was varied in the range 300-360mT.

2.2.2 XAS

X-ray Absorption Spectroscopy measurements at the Fe K-edge (7,112 eV) were performed at the BM23 bending magnet beamline at the European Radiation Synchrotron Facility (ESRF, Grenoble, France). Two Rh-coated mirrors, located before and after the double crystal monochromator with respect to the beam direction, were used for efficient harmonics rejection, collimation, and vertical focusing of the beam. A sagittal focusing system provided a beam intensity of 10^{10} photons s^{-1} at 12 keV, and a beam size on the sample of approximately 300 × 200 µm (H × V). The beam energy was selected using a couple of Si(220) crystals; with this experimental setup, the energy resolution is estimated to be ~0.4 eV. A Fe metallic foil was used to calibrate the monochromator energy. The same foil was mounted downstream to the sample and measured simultaneously with the sample spectra at each energy scan to monitor possible unphysical energy shifts during consecutive measurements. Due to the high dilution level of Fe in the samples, the spectra were recorded in fluorescence mode using a high-throughput 13-element solid state Ge detector (Canberra, St Quentin Yvelines, France). When necessary, the optimization described in Maurizio et al., 2009 were used to minimize the contribution from the elastic peak [20]. Spectra of Fe reference compounds were acquired in transmission mode using two ionization chambers to measure the incoming and transmitted X-ray beam. Up to five consecutive scans were acquired for each sample to increase statistics. For all samples, no changes were observed in the spectral features between consecutive scans, indicating that beam-induced redox variations did not occur. The XANES spectra were background subtracted, normalized, and aligned using the spectrum of the metallic Fe foil as a reference. The EXAFS signals were obtained by subtracting a spline curve mimicking the atomic background from the extended part of the spectra. Preliminary data reduction and extraction of the EXAFS signal were performed using the IFEFFIT software package [21]. The refinement of the local structure around the absorber atom (Fe) was obtained using the Estra-Fitexa software package [22], which uses photo-electron scattering functions calculated by the FEFF6 software [23]. Principal Component Analysis (PCA) [24], which allows to assess the minimum number of factors necessary to reconstruct the experimental spectra, was applied to both the absorption and the EXAFS spectra. A dedicated module included in the Sixpack software package was used to perform PCA [25]. Linear Combination Fitting of the experimental XANES spectra using a set of reference compounds spectra was also performed using the dedicated module included in the IFEFFIT software package. The analysis of the pre-edge features of the XANES Fe K-edge spectra was carried out following a consolidated approach reported in the literature [26,27]. The pre-edge peak envelope of the calibrated and normalized XAS spectra of the investigated samples was fitted by means of two Gaussian components, after subtraction of the edge ramp background, which was mimicked by a spline function. The number of the components used in the fit was chosen as the minimum necessary to reproduce the peaks clearly identifiable in the experimental spectra. The Gaussian function was found to fit adequately the experimental profiles in some preliminary tests and was thus preferred to the conventional Pseudo-Voigt profile function because of the lower number of parameters to be

refined. All operations associated to the fit decomposition were carried out using the Microcal Origin 9 software. No constraints were applied to the peak position, width, and intensity. Statistical tests performed over the whole dataset of refined parameters (6 parameters describing two peaks evaluated for 45 spectra) allowed to sort out the absolute uncertainties of 0.09 eV for the energy value and 0.003 (arbitrary units, a.u.) for the peak areas (net intensity of the two Gaussian components). This results in relative uncertainties of the order of 10^{-3} % and 5 % for the for energy and intensity determinations, respectively.

3. Results

3.1 EPR spectroscopic results

EPR spectroscopy is a technique able to detect the presence of unpaired electrons belonging either to unfilled d levels (as in transition metals) or to radical species. An exemplar EPR room temperature spectrum of the ET ash sample is shown in Figure 2a. The spectrum is characterized by the presence of a single, broad, asymmetric, and unstructured intense signal with centered in the range 300-350mT. The EPR samples spectra have variable combinations of signal asymmetry and broadness, but share the presence of a single intense signal, without secondary lines or hyperfine structure. The average Fe content provided by [17] (about 11wt%), the peculiar signal intensity, and the absence of an hyperfine structure, suggest the presence of Fe(III) [28]. At 35K, two main new features are observed (Figure 2b): i) A signal at about 160mT (labelled as “I” in Figure 2b), with a line width of ~25mT; this signal can be safely attributed to isolated Fe(III) ions in rhombic distortion, as it usually occurs in minerals and glasses if the concentration of paramagnetic ions is low enough to prevent a significant contribution of the exchange interaction [28–30]. ii) The main signal of the spectrum, which is still an intense, asymmetric, and broad band centered at 275mT (labelled as “II” in Figure 2b); this band is attributed to the same Fe(III) species observed in the room temperature spectrum (Figure 2a).

From the comparison of the room and low temperature spectra, it can be concluded that the peak position shifts with temperature from ~325 to ~275mT, and that the width of the signal is also changing, increasing from ~80 to ~150mT. This behavior cannot be associated to an isolated paramagnetic ion, for which the peak position is, at a first approximation, independent on the temperature, while the relative width is slightly decreasing with lowering the temperature [28]. Thus, the main signal observed in the EPR spectra of the investigated samples may be attributed to Fe(III) in a magnetic concentrated environment. In fact, the shift of the line position and the increase of its width with decreasing temperature, has already been observed for the latter species [31].

Further indications are obtained from the HFEPR measurements, an example of which is shown in the Figure 2c. In the spectrum of ET acquired at 190GHz and 298K only a very weak signal centered at B ~ 6.79T and with a width of ~20mT was observed. This is likely attributed to the higher detection limit of the HFEPR instrumentation compared to the conventional EPR set up (HFEPR was operated in the single pass mode, i.e. no resonance of the microwave radiation was attained). Another reason for the lack of a stronger signal may be that the peak intensity (of signal II) decreased because its relative susceptibility spread over a wider field range. In addition, the resonance modes of the permanent magnetic phases in Fe(III) oxide compounds exhibit a field- and frequency- dependence that can hinder the detection of some

signals [32].

For these reasons, the signal observed in Figure 2c may be attributed to Fe(III) occurring in a third aggregation state with respect to those reported in the Figures 2a and 2b. The Fe(III) oxide clusters that could give rise to this signal should have a size of the order of 2nm. Moreover, this signal is independent on temperature [31]. The onset of long range magnetic correlation has been ascertained at least for hematite (Fe_2O_3) for such small clusters [33].

The ET sample was also investigated by EchoEPR, in the same magnetic field range of Figure 2b and at 35 K, by using a 16-32 ns Hahn decay pulse sequence, but no signals were detected. Thus, the three previously described species were not selected by the used sequence. This is in agreement with the presence of concentrated Fe(III) species. Under the operated conditions, the EchoEPR set up is in fact able to detect only isolated species, not interacting with other paramagnetic species in their surroundings. On the other hand, isolated rhombic Fe(III) is not detected after the pulse sequence due to crystal field effects [34]. The presence of inorganic radicals cannot be detected with conventional EPR measurements due to the superposition of the very intense signal of concentrated Fe(III) species. In contrast, EchoEPR is not able to detect signals from concentrated Fe(III) species, making it possible to reveal those from radical species. Thus, the observed lack of contributions of inorganic radical signals to the EchoEPR spectra suggests that there these species are not present in the investigated samples (within the detection limit of ~10^{14} atoms/cm^3 [35]).

3.2 XAS results

3.2.1 Pre-edge

The common approach to determine the average oxidation state of Fe has long been that to compare the position of the absorption edge to that of Fe reference compounds. More recently, Wilke et al. (2001) [26] have shown that the shape of the Fe absorption K-edge is strongly influenced by the Fe oxidation state and coordination environment, i.e. the nearest-neighbor species and their geometry around the absorber atom (tetrahedral, octahedral, or other). They demonstrated that the relevant parameter to infer the oxidation state of Fe is the energy position of the centroid of the pre-edge feature(s), which is related to 1s–3d or 4d electronic transitions, while the average coordination number can be inferred by the intensity or integrated area of the centroid. This analysis can be performed provided that an energy *vs.* oxidation state/coordination number calibration curve is built using the energy position and intensity of the centroid of the pre-edge peak(s) of Fe(II) and Fe(III) reference compounds spectra (Figure 3b). Following this approach, we showed that all the X-ray absorption samples spectra exhibit a two-peak Pre-Edge (PE) feature (Figure 3a). Most of the pre-edge peak data can be modelled with an admixture of the integrated centroid peak area of crystalline Fe(II) (and possibly also glassy Fe(II)) and glassy Fe(III) endmembers (Figure 3b), resulting in $Fe(III)/Fe_{tot}$ ratio varying in the range 0.14(5) - 0.36(5). The analysis of the aliquots of the same sample with different granulometry (>850, <850, and <63μm) shows that the $Fe(III)/Fe_{tot}$ ratio increases with lowering the particles size (see Table 1, Supplementary Material). However, the CIT and CIT_{90} samples (Group C in the following, see Table 2) may also be modelled using integrated centroid peak area of glassy Fe(II) and

crystalline Fe(III) endmembers. As a result, the Fe redox estimated for the Group C samples may suffer of a higher error.

A clearer trend is depicted for the ET series (Figure 4a). For these samples, it was possible to model the data by using a combination of two endmember: a pre-edge peak integrated area value representative of glassy Fe(II) and another representative of crystalline Fe(III). In this model, Fe(II) was found to have a coordination number intermediate between 4 and 5, which is compatible with its presence in the glassy phase, whereas Fe(III) has higher coordination number, compatible with crystalline phases. The $Fe(III)/Fe_{tot}$ ratio ranges between 0.26(5) in ET1 (500-1000μm) and 0.53(5) in ET4 (63-125μm), with the ET_{tot} sample having an average value of 0.35. This suggests that the Fe(III) content increases with decreasing particle size, as highlighted in Figure 4b). This trend may be ascribed to an increased amount of Fe crystalline phases in smaller particles, which, in agreement with Barone et al. [17], would occur near the particle surface.

3.2.2 XANES

Principal Component Analysis (PCA) was applied to the 45 XANES spectra to help determining the minimum number of components necessary to reconstruct all experimental spectra. The results indicated that four components are required to reconstruct satisfactorily the spectra. Accordingly, at a visual inspection the XANES spectra can be divided in three groups labelled A, B, and C (see Table 2), with minor differences at the pre-edge and main absorption peaks, which probably reflect the presence of variable relative amounts of different Fe local environments. One sample spectrum (MAS) has unique features and cannot be included in the above groups. Average XANES spectra of representative samples belonging to the A, B, and C groups, and of the MAS sample, are reported in Figure 5a.

Linear Combination Fitting (LCF) was attempted to reveal the Fe speciation by fitting the experimental spectra with a linear combination of Fe reference compound spectra. The set of Fe references (Figure 1, Supplementary Material) included magnetite, hematite, and ferrihydrite [36,37], pyrite and Fe-sulfate [38], fayalite and almandine [39], and two silicate glasses: natural cambodianite, containing Fe(II) with an average coordination number intermediate between 4 and 5 [27], and the phonolite synthetic glass OIph-1A, containing tetrahedral Fe(III) [40]. This is in agreement with the PCA analysis that suggested that four components are required to reproduce each experimental spectrum satisfactorily. The results of LCF show that all the spectra can be satisfactorily fitted with variable amounts of magnetite (nominally 1/3 tetra-coordinated Fe^{2+} and 2/3 hexa-coordinated Fe^{3+}), Fe-sulfate (Fe^{2+} in octahedral coordination), cambodianite (tetra- and penta-coordinated Fe^{2+}), and phonolite glasses (OIPh-1a, tetra-coordinated Fe^{3+}). Considering the excellent match with the experimental spectra (see Figure 5a), the results of the linear combinations are likely to reflect the actual Fe speciation, which can be described by an admixture of variable amounts of silicate glasses containing Fe inclusions, Fe-oxides, and Fe(II)-sulfate phases (Table 2). The composition of group B samples (Table 2), would suggest that lower granulometries (<125μm) are associated with a lower presence of Fe(II)-sulfate species. Finally, the Fe speciation seems to be not affected by leaching experiments, as suggested by the similar composition found for leached and unleached samples (Table 2).

3.2.3 EXAFS

Structural refinement of the Fe local environment (up to 4-5Å from the absorber atom) was performed by least square minimization of the

EXAFS signal extracted from the extended part absorption spectra (> ~150eV from the Fe absorption edge) of the representative spectra of Group A, B, and C, and of MAS. The refinements were performed in the k-space to avoid artefacts introduced by Fourier filtering. After trying different models, satisfactory structural refinements were obtained by setting a model with two first shell (near-neighbor) Fe-O bond distances (Fe-O_1 and Fe-O_2). The coordination number (CN) of the shortest distance was set to 4, as in FeO tetrahedral, and the longest one to 6 (FeO octahedra). For group A and B, a weight factor, *x*, was let free to vary during the minimizations to estimate the relative amounts of the two Fe-O contributions (*x(*Fe-O_1) and (1-*x*)(Fe-O_2)). The magnetite reference was fitted using the same model. For each shell, the coordination numbers (CN), bond distances (R), and Debye-Waller factors (σ^2, i.e. the thermal vibrations and structural disorder), were free parameters in the minimizations. Other free parameters, common to all shells, were the energy shift with respect to the theoretical scattering functions (E_0). The XAS amplitude reduction factor (S_0^2) was set to 0.9 for all samples. For the silicate glass references, we refer to the structural refinements reported in Giuli et al. [27,40]. The refined average Fe-O bond distances of all samples were similar: ~1.89 Å (Fe-O_1) and ~2.05 Å (Fe-O_2). These values are similar to those of the magnetite reference (Table 3). The Fe-O_1 bond distance matches with that of tetrahedral Fe(III), which is in the range 1.85 – 1.88 Å in glasses [39,40] and 1.85 – 1.86 Å in crystalline phases [42–44]. The longest bond distance (Fe-O_2) is in agreement with the average bond distance of Fe in octahedral sites (3 Fe-O at 1.94 Å and 3 Fe-O at 2.12 Å), as reported by [45] for hematite. The fraction of octahedral Fe sites ranged between 0.3 and 0.5 (Table 3), suggesting a spinel-like environment, although the error on the weight parameter (*x*) can reach 50% of its value. However, it is not possible to assign the first shell distances to specific species, because LCF results showed that they arise from an admixture of Fe-oxide species with similar Fe-O bond distances and coordination numbers. The EXAFS data reveal a clear evidence of contributions arising from Fe coordination shells at longer distance from the absorber atom (Figure 5, c and d). These shells were fitted with two Fe-Fe shells with average refined bond distances of ~2.99 and ~3.44 Å (Table 3). Due to the strong correlation with the Debye-Waller factors, the refined coordination numbers of these shells are not reliable. No contribution from a Fe-Si coordination shell was found in any of the samples. This may be due to the relatively strong contribution of the Fe-Fe shells, which may hinder the weaker Fe-Si contribution. The refinement of the Group C and MAS spectra can be significantly improved by adding an Fe-S contribution at about 3.01 Å (Table 3). This is in agreement with the results of the LCF analysis, which indicate a higher amount of Fe(II)-sulfate in these samples. The EXAFS signals (experimental and fit) of the analyzed samples are shown in Figure 5c, and the Fourier Transform of the experimental data and fit curves are shown Figure 5d.

4. Discussion

The results of the present study are in agreement with the recent literature, and they can be interpreted as being the result of the intrinsic redox features of the magma into the chamber, followed by a modification occurring inside the eruption plume at high temperature. Ayris and Delmelle [1] proposed a model where the ejected volcanic ashes undergo to successive evolution stages. In this model, the ash samples studied in this work correspond to the evolution stages II and III, i.e. those subjected to subaerial volcanic and atmospheric modifications. Since ash samples were sampled immediately after the eruption events, any weathering processes in atmosphere, which effects start to be

appreciable few hours after the event [46], can be excluded.

The Fe(III) speciation depicted by EPR is variegate, ranging from isolated to clustered in nanoparticles, in agreement with Calvari et al. [11], to larger magnetic particles. In particular, combined EPR and HFEPR revealed that Fe(III) occurs in at least two different phases, most of it being included in the volcanic glass, in agreement with the results of Ayris et al. and Calvari et al. [1,11], and the remaining hosted in a magnetic phase, probably an Fe oxide. HFEPR analyses also suggested that a fraction of superparamagnetic Fe is hosted in crystallites with dimensions that do not allow a multi-domain magnetic structure to be established.

The PE and the LCF analyses of the XANES spectra revealed the coexistence of Fe(II) and Fe(III) species in a variety of different coordination environments. Fe(II) and Fe(III) occur in an almost constant ratio in the raw bulk samples (with the Fe(III)/Fe_{tot} ranging between 0.14 and 0.36 with an average of 0.27 and a standard deviation of 0.06), whereas significant changes were evidenced as a function of particle granulometry, especially for the ET and BIA samples. In particular, the relative Fe(III) fraction increases with decreasing particle size, and is likely to be enriched close to the particle rim. This is supported by the fact that almost all of the finest samples aliquots (<63 μm and <125 μm) can be included in a separate group with different spectral features (group B, Table 2), with respect to the larger particle size samples aliquots (Group A, C, and MAS, Table 2). In agreement with the EPR results, shell fitting EXAFS refinements revealed the presence of a next neighbor Fe coordination shell, which suggests that Fe may segregate in Fe crystalline phases. Finally, XAS results also showed that the 30, 90, and 180 minutes long leaching experiments with water did not affect significantly the Fe oxidation state and speciation.

Altogether, XAS and EPR data depict a mixed Fe speciation, where variable amounts of Fe-oxides and Fe(II)-sulfate species coexist with Fe inclusions of different nature in the bulk glassy phase. This picture is partly different from that of the grains surface, which was revealed in our previous work by XPS and TEM analyses on the same samples [17]. For example, in the previous work a poor correlation between Fe and S was detected, while Fe(II)-sulfate species have been detected in the present work. This can be explained by the fact that, due the higher penetration depth of hard X-rays, XAS probes also the bulk of the samples. Conversely, XPS and TEM are only able to probe a thin surface layer (<250 nm).

The presence of Fe(II)-sulfate species detected by XAS can be explained by assuming that, during an unrest period and/or ash eruption, the ash plume and the gas plume coexist, the latter being rich in SO_2 [47,48]. The SO_2 present in the gas plume reacts with the water vapour present in the atmosphere, accordingly to the overall reaction:

$SO_2 + H_2O = H_2SO_3$, $H_2SO_3 + 0.5O_2 = H_2SO_4$

The Fe(II) contained in the volcanic ash is likely to react with the product of SO_2 hydration, thus producing Fe(II)-sulfites/sulfates; the Fe(III), on the other hand, is more likely to stabilize as oxides. XAS data also show that the amount of Fe(II)-sulfate is generally lower for smaller grain sizes (see Group B in Table 2). For smaller particles, the fraction of the XAS signal originating from the particles rim is larger than that arising from larger particles, where the signal from the bulk predominates. Therefore, the observed Fe(II)-sulfate trend with grain size can be interpreted as being the evidence of a decreasing Fe(II)-sulfate amount in the core-to-rim direction. As pointed out above, XAS results also

suggest an opposite trend for Fe(III), which, as stated above, mainly occurs in the form of Fe-oxide (as in the ET series), or as network of FeO_4 tetrahedral units forming within the glass matrix.

The above findings can be interpreted by assuming that in a first stage, SO_2 reacts with Fe(II) in anoxic conditions. When the ash plume is in contact with O_2, Fe(II) oxidation to Fe(III) occurs, eventually forming crystalline Fe-oxides phases. It is also worth noting that, because of the lack of a Fe(II)-sulfite reference, it was not possible to discriminate between Fe(II)-sulfate and Fe(II)-sulfite species in the samples. However, thermodynamic considerations support the presence of magnetite/magnesioferrite and Fe(II)-sulfate phases, while the formation of hematite and Fe(III)-sulfate is unfavored [49, and references therein]. This is compatible with the $Fe(III)/Fe_{tot}$ range values, which indicate a predominant amount of reduced Fe species.

All the above findings are compatible with the scenario proposed in our previous study [17], in which ash samples exhibit a complex variability in the rim-to-core structure. Namely, an external rim mainly consisting of Fe-free crystalline species (e.g. Ca sulfate and fluoride) encloses an inner rim where the total Fe concentration is enriched with respect to the glassy core of the particle. The Fe excess in this internal rim is sensitive to the in-plume oxidation, which is confirmed by the pre-edge analysis of the XANES spectra, indicating that the amount of Fe(III) increases when the particle size decreases. In agreement with [1,50,51], a preferential oxidation pathway in the smaller particles can be attributed to a diffusion limited process, which results in an Fe(III)-rich rim of ~50-200 nm in size. The effect of this pathway on the average Fe redox state is higher for smaller particles. According to the findings of Ayris et al. and Barone et al. [1,17], the Fe(III) excess may drive the formation of Fe crystalline phases. The present EXAFS investigation also suggests that the process of Fe segregation in crystalline phases is not occurring alone, since clustering of Fe in Fe-rich domains was detected in the samples. Together, the lack of Fe leaching observed in the previous work [17], and the decrease of the Fe(II)-sulfate phase in the core-to-rim direction revealed by XAS data, suggest that the sulfur-bearing phase may occur in an inner shell, surrounded by the Fe-oxide shell, and by the external rim of Fe-free crystalline species. On the basis of this scenario, we believe that the specific surface features of the Etna's ashes may prevent direct exposure to most mobile and toxic Fe(II). In particular, considering the breathable fraction, which has a mean aerodynamic diameter of less than 4μm, the Fe(III) rim at the particles surface should prevent direct interaction between Fe(II), which would be mainly contained in the inner part of the ash grains, and the biological tissues.

However, at least two surface modification processes may modify the post-eruption composition of the ash in a temporal range between some tens of hours to few weeks. Andronico et al. [52] pointed out that vehicular traffic in the urban areas close to the volcano (mainly pertaining to the nearby Catania city), not only favors re-suspension and remobilization of the ash particles, but also lead to a decrease of the mean size of their granulometric distribution, which in turns leads to the formation of new surfaces. As a result, soluble Fe(II) may be present also at the particle surface, posing an health threat upon prolonged exposure. In addition, a mechanical activation of the ashes could also induce the formation of surface radicals. According to Maters et al. [46], a further source of surface modification would initiate few hours after the eruptive event: the ash particles may undergo severe weathering under evaporation/condensation processes in the atmosphere, and consequent pH changes, which lead to the occurrence of Fe(II) in close contact to newly formed particle surfaces. Therefore, as also

pointed out by other authors [2], the potential toxicity of Etna ash particles must be carefully evaluated, especially in presence of prolonged exposure.

Author contributions

Fabrizio Bardelli, Gabriele Giuli, Francesco Di Benedetto, Giordano Montegrossi, Germana Barone, Paolo Mazzoleni: Conceptualization, Writing - Original Draft, Writing - Review & Editing. **Giordano Montegrossi, Valentina Rimondi:** Writing - Review & Editing. **Fabrizio Bardelli, Gabriele Giuli, Francesco Di Benedetto**: Formal Analysis. **Pilar Costagliola, Luca Pardi, Francesco Di Benedetto, Giordano Montegrossi, Maurizio Romanell**i: Investigation. **Germana Barone, Paolo Mazzoleni**: Resources

,

Declaration of interests

The authors declare that they have no known competing financial interests or personal relationships that could have appeared to influence the work reported in this paper.

Acknowledgements

This work was supported by the University of Catania - FIR 2014, and by MIUR PNR - AGM for CuHe CUP E66C18000380005 - RNA-COR 605359.

.

REFERENCES

[1] P. Ayris, P. Delmelle, Volcanic and atmospheric controls on ash iron solubility: A review, Phys. Chem. Earth. 45–46 (2012) 103–112. https://doi.org/10.1016/j.pce.2011.04.013.

[2] C.J. Horwell, I. Fenoglio, B. Fubini, Iron-induced hydroxyl radical generation from basaltic volcanic ash, Earth Planet. Sci. Lett. 261 (2007) 662–669. https://doi.org/10.1016/j.epsl.2007.07.032.

[3] F. Bardelli, E. Cattaruzza, F. Gonella, G. Rampazzo, G. Valotto, Characterization of road dust collected in Traforo del San Bernardo highway tunnel: Fe and Mn speciation, Atmos. Environ. 45 (2011) 6459–6468. https://doi.org/10.1016/j.atmosenv.2011.07.035.

[4] S. Shoji, T. Takahashi, Environmental and agricultural significance of volcanic ash soils, Glob. Environ. Res. Ed. 6 (2002) 113–135. http://www.airies.or.jp/attach.php/6a6f75726e616c5f30362d32656e67/save/0/0/06_2-12.pdf.

[5] A. Aiuppa, P. Allard, W. D'Alessandro, A. Michel, F. Parello, M. Treuil, M. Valenza, Mobility and fluxes of major, minor and trace metals during basalt weathering and groundwater transport at Mt. Etna volcano (Sicily), Geochim. Cosmochim. Acta. 64 (2000) 1827–1841. https://doi.org/10.1016/S0016-7037(00)00345-8.

[6] D.S. Su, X. Chen, X. Liu, J.J. Delgado, R. Schlögl, A. Gajović, Mount-Etna-Lava-Supported Nanocarbons for Oxidative Dehydrogenation Reactions, Adv. Mater. 20 (2008) 3597–3600. https://doi.org/10.1002/adma.200800323.

[7] D. Andronico, R.A. Corsaro, Lava fountains during the episodic eruption of South-East Crater (Mt. Etna), 2000: Insights into magma-gas dynamics within the shallow volcano plumbing system, Bull. Volcanol. 73 (2011) 1165–1178. https://doi.org/10.1007/s00445-011-0467-y.

[8] B. Behncke, S. Branca, R.A. Corsaro, E. De Beni, L. Miraglia, C. Proietti, The 2011-2012 summit activity of Mount Etna: Birth, growth and products of the new SE crater, J. Volcanol. Geotherm. Res. 270 (2014) 10–21. https://doi.org/10.1016/j.jvolgeores.2013.11.012.

[9] A. Bonaccorso, S. Calvari, A. Linde, S. Sacks, Eruptive processes leading to the most explosive lava fountain at Etna volcano: The 23 November 2013 episode, Geophys. Res. Lett. 41 (2014) 4912–4919. https://doi.org/10.1002/2014GL060623.

[10] M. Aloisi, A. Bonaccorso, F. Cannavò, G.M. Currenti, Coupled Short- and Medium-Term Geophysical Signals at Etna Volcano: Using Deformation and Strain to Infer Magmatic Processes From 2009 to 2017, Front. Earth Sci. 6 (2018). https://doi.org/10.3389/feart.2018.00109.

[11] S. Calvari, F. Cannavò, A. Bonaccorso, L. Spampinato, A.G. Pellegrino, Paroxysmal Explosions, Lava Fountains and Ash Plumes at Etna Volcano: Eruptive Processes and Hazard Implications, Front. Earth Sci. 6 (2018). https://doi.org/10.3389/feart.2018.00107.

[12] M. Viccaro, M. Giuffrida, F. Zuccarello, M. Scandura, M. Palano, S. Gresta, Violent paroxysmal activity drives self-feeding magma replenishment at Mt. Etna, Sci. Rep. 9 (2019). https://doi.org/10.1038/s41598-019-43211-9.

[13] F. Marchese, M. Neri, A. Falconieri, T. Lacava, G. Mazzeo, N. Pergola, V. Tramutoli, The Contribution of Multi-Sensor Infrared Satellite Observations to Monitor Mt. Etna (Italy) Activity during May to August 2016, Remote Sens. 10 (2018) 1948. https://doi.org/10.3390/rs10121948.

[14] S. Gambino, M. Aloisi, G. Di Grazia, G. Falzone, A. Ferro, G. Laudani, Ground Deformation Detected by Permanent Tiltmeters on Mt. Etna Summit: The August 23-26, 2018, Strombolian and Effusive Activity Case, Int. J. Geophys. 2019 (2019). https://doi.org/10.1155/2019/1909087.

[15] F. Cannavo', M. Sciotto, A. Cannata, G. Di Grazia, An Integrated Geophysical Approach to Track Magma Intrusion: The 2018 Christmas Eve Eruption at Mount Etna, Geophys. Res. Lett. 46 (2019) 8009–8017. https://doi.org/10.1029/2019GL083120.

[16] D. Andronico, S. Scollo, M.D. Lo Castro, A. Cristaldi, L. Lodato, J. Taddeucci, Eruption dynamics and tephra dispersal from the 24 November 2006 paroxysm at South-East Crater, Mt Etna, Italy, J. Volcanol. Geotherm. Res. 274 (2014) 78–91. https://doi.org/10.1016/j.jvolgeores.2014.01.009.

[17] G. Barone, P. Mazzoleni, R.A. Corsaro, P. Costagliola, F. Di Benedetto, E. Ciliberto, D. Gimeno, C. Bongiorno, C. Spinella, Nanoscale surface modification of Mt. Etna volcanic ashes, Geochim. Cosmochim. Acta. 174 (2016) 70–84. https://doi.org/10.1016/j.gca.2015.11.011.

[18] C. Stewart, C. Horwell, G. Plumlee, S. Cronin, P. Delmelle, P. Baxter, J. Calkins, D. Damby, S. Morman, C. Oppenheimer, Protocol for analysis of volcanic ash samples for assessment of hazards from leachable elements, (2013) 22.

[19] R.A. Corsaro, Dynamics of 2004–2005 Mt. Etna effusive eruption as inferred from petrologic monitoring, Geophys. Res. Lett. 32 (2005) L13302. https://doi.org/10.1029/2005GL022347.

[20] C. Maurizio, M. Rovezzi, F. Bardelli, H. G. Pais, F. D'Acapito, Setup for optimized grazing incidence x-ray absorption experiments on thin films on substrates, Rev. Sci. Instrum. 80 (2009) 063904. https://doi.org/10.1063/1.3155791

[21] B. Ravel, M. Newville, ATHENA, ARTEMIS, HEPHAESTUS: data analysis for X-ray absorption spectroscopy using IFEFFIT., J. Synchrotron Radiat. 12 (2005) 537–41. https://doi.org/10.1107/S0909049505012719.

[22] C. Meneghini, F. Bardelli, S. Mobilio, ESTRA-FitEXA: A software package for EXAFS data analysis, Nucl. Instruments Methods Phys. Res. Sect. B Beam Interact. with Mater. Atoms. 285 (2012) 153–157. https://doi.org/10.1016/j.nimb.2012.05.027.

[23] J.J. Rehr, R.C. Albers, S.I. Zabinsky, High-order multiple-scattering calculations of x-ray-absorption fine structure, Phys. Rev. Lett. 69 (1992) 3397–3400. https://doi.org/10.1103/PhysRevLett.69.3397.

[24] E.R. Malinowski, Theory of the distribution of error eigenvalues resulting from principal component analysis with applications to spectroscopic data, J. Chemom. 1 (1987) 33–40. https://doi.org/10.1002/cem.1180010106.

[25] S.M. Webb, SIXpack: A graphical user interface for XAS analysis using IFEFFIT, Phys. Scr. T. T115 (2005) 1011–1014. https://doi.org/10.1238/Physica.Topical.115a01011.

[26] M. Wilke, F. Farges, P.E. Petit, G.E. Brown, F. Martin, Oxidation state and coordination of Fe in minerals: An FeK- XANES spectroscopic study, Am. Mineral. 86 (2001) 714–730.

[27] G. Giuli, G. Pratesi, C. Cipriani, E. Paris, Iron local structure in tektites and impact glasses by extended X-ray absorption fine structure and high-resolution X-ray absorption near-edge structure spectroscopy, Geochim. Cosmochim. Acta. 66 (2002) 4347–4353. https://doi.org/10.1016/S0016-7037(02)01030-X.

[28] B.A. Goodman, J.B. Raynor, Electron Spin resonance of transition metal complexes, Adv. Inorg. Chem. Radiochem. 13 (1970) 135–362. https://doi.org/10.1016/S0065-2792(08)60336-2.

[29] A. Zoleo, M. Brustolon, A. Barbon, A. Silvestri, G. Molin, S. Tonietto, Fe(III) and Mn(II) EPR quantitation in glass fragments from the palaeo-Christian mosaic of St. Prosdocimus (Padova, NE Italy): Archaeometric and colour correlations, J. Cult. Herit. 16 (2015) 322–328. https://doi.org/10.1016/j.culher.2014.07.005.

[30] E. Balan, T. Allard, B. Boizot, G. Morin, J.P. Muller, Structural Fe3+ in natural kaolinites: New insights from electron paramagnetic resonance spectra fitting at X and Q-band frequencies, Clays Clay Miner. 47 (1999) 605–616. https://doi.org/10.1346/CCMN.1999.0470507.

[31] C. Carbone, F. Di Benedetto, C. Sangregorio, P. Marescotti, L.A. Pardi, L. Sorace, Multifrequency EMR and Magnetic Characterization of Synthetic Powdered Hematite, J. Phys. Chem. C. 112 (2008) 9988–9995. https://doi.org/10.1021/jp712045s.

[32] A.H. Morrish, Canted antiferromagnetism : hematite, World Scientific, 1994.

[33] Amin, Arajs, Morin temperature of annealed submicronic alpha -F2O3 particles., Phys. Rev. B. Condens. Matter. 35 (1987) 4810–4811. https://doi.org/10.1103/physrevb.35.4810.

[34] A. Zoleo, C. Bortolussi, M. Brustolon, Echo detected EPR as a tool for detecting radiation-induced defect signals in pottery, Radiat. Meas. 46 (2011) 676–679. https://doi.org/10.1016/j.radmeas.2011.06.012.

[35] F. Capacci, F. Carnevale, F. Di Benedetto, eds., Silice Libera Cristallina nei luoghi di lavoro, 2010.

[36] A. Voegelin, R. Kaegi, J. Frommer, D. Vantelon, S.J. Hug, Effect of phosphate, silicate, and Ca on Fe(III)-precipitates formed in aerated Fe(II)- and As(III)-containing water studied by X-ray absorption spectroscopy, Geochim. Cosmochim. Acta. 74 (2010) 164–186. https://doi.org/10.1016/j.gca.2009.09.020.

[37] F. d'Acapito, S. Mazziotti Tagliani, F. Di Benedetto, A. Gianfagna, Local order and valence state of Fe in urban suspended particulate matter, Atmos. Environ. 99 (2014) 582–586. https://doi.org/10.1016/j.atmosenv.2014.10.028.

[38] F. Bardelli, E. Cattaruzza, F. Gonella, G. Rampazzo, G. Valotto, Fe and Mn speciation in road dust particles by XAS, J. Phys. Conf. Ser. 190 (2009) 012192. https://doi.org/10.1088/1742-6596/190/1/012192.

[39] F. Di Benedetto, F. D'Acapito, F. Capacci, G. Fornaciai, M. Innocenti, G. Montegrossi, W. Oberhauser, L.A. Pardi, M. Romanelli, Variability of the health effects of crystalline silica: Fe speciation in industrial quartz reagents and suspended dusts-insights from XAS spectroscopy, Phys. Chem. Miner. 41 (2014) 215–225. https://doi.org/10.1007/s00269-013-0640-2.

[40] G. Giuli, E. Paris, K.U. Hess, D.B. Dingwell, M.R. Cicconi, S.G. Eeckhout, K.T. Fehr, P. Valenti, XAS determination of the Fe local environment and oxidation state in phonolite glasses, Am. Mineral. 96 (2011) 631–636. https://doi.org/10.2138/am.2011.3464.

[41] G. Giuli, R. Alonso-Mori, M.R. Cicconi, E. Paris, P. Glatzel, S.G. Eeckhout, B. Scaillet, Effect of alkalis on the Fe oxidation state and local environment in peralkaline rhyolitic glasses, Am. Mineral. 97 (2012) 468–475. https://doi.org/10.2138/am.2012.3888.

[42] F. Bosi, U. Hålenius, H. Skogby, Crystal chemistry of the magnetite-ulvöspinel series, Am. Mineral. 94 (2009) 181–189. https://doi.org/10.2138/am.2009.3002.

[43] G. Giuli, E. Paris, Z. Wu, M.F. Brigatti, G. Cibin, A. Mottana, A. Marcelli, Experimental and theoretical XANES and EXAFS study of tetra-ferriphlogopite, Eur. J. Mineral. 13 (2001) 1099–1108. https://doi.org/10.1127/0935-1221/2001/0013-1099.

[44] G. Giuli, M.R. Cicconi, E. Paris, The [4]Fe3+-O distance in synthetic kimzeyite garnet, Ca3Zr2[Fe2SiO12], in: Eur. J. Mineral., E. Schweizerbart'sche Verlagsbuchhandlung, 2012: pp. 783–790. https://doi.org/10.1127/0935-1221/2012/0024-2206.

[45] N. Pailhé, A. Wattiaux, M. Gaudon, A. Demourgues, Impact of structural features on pigment properties of α-Fe 2O3 haematite, J. Solid State Chem. 181 (2008) 2697–2704. https://doi.org/10.1016/j.jssc.2008.06.049.

[46] E.C. Maters, P. Delmelle, S. Bonneville, Atmospheric Processing of Volcanic Glass: Effects on Iron Solubility and Redox Speciation, Environ. Sci. Technol. 50 (2016) 5033–5040. https://doi.org/10.1021/acs.est.5b06281.

[47] D.D. Donne, A. Aiuppa, M. Bitetto, R. D'Aleo, M. Coltelli, D. Coppola, E. Pecora, M. Ripepe, G. Tamburello, Changes in SO2 Flux regime at mt. etna captured by automatically processed ultraviolet camera data, Remote Sens. 11 (2019). https://doi.org/10.3390/rs11101201.

[48] R. D'aleo, M. Bitetto, D.D. Donne, M. Coltelli, D. Coppola, B.M. Kilbride, E. Pecora, M. Ripepe, L.C. Salem, G. Tamburello, A. Aiuppa, Understanding the SO 2 degassing budget of Mt Etna's paroxysms: First clues from the december 2015 sequence, Front. Earth Sci. 6 (2019) 1–23. https://doi.org/10.3389/feart.2018.00239.

[49] G. Hoshyaripour, Modulation of Ash Iron Solubility in Volcanic Eruption Plumes, PhD Dissertation at University of Hamburg, 2013, 102pp.

[50] Y. Yamanoi, S. Takeuchi, S. Okumura, S. Nakashima, T. Yokoyama, Color measurements of volcanic ash deposits from three different styles of summit activity at Sakurajima volcano, Japan: Conduit processes recorded in color of volcanic ash, J. Volcanol. Geotherm. Res.

178 (2008) 81–93. https://doi.org/10.1016/j.jvolgeores.2007.11.013.

[51] G. Hoshyaripour, M. Hort, B. Langmann, P. Delmelle, Volcanic controls on ash iron solubility: New insights from high-temperature gas-ash interaction modeling, J. Volcanol. Geotherm. Res. 286 (2014) 67–77. https://doi.org/10.1016/j.jvolgeores.2014.09.005.

[52] D. Andronico, P. Del Carlo, PM_{10} measurements in urban settlements after lava fountain episodes at Mt. Etna, Italy: pilot test to assess volcanic ash hazard to human health, Nat. Hazards Earth Syst. Sci. 16 (2016) 29–40. https://doi.org/10.5194/nhess-16-29-2016.

Table 1. List of the investigated samples.

Sample label*	Particles diameter (μm)	Leaching (minutes)	Sampling locality	Eruption episode DD/MM/YYYY	Distance from NSEC** (km)
LIN	<850	-	Linguaglossa	28/11/2013	15
LIN>850	>850	-			
LIN_{90}	<850	90			
CIT	<850	-	Citelli	28/11/2013	6
CIT>850	>850	-			
CIT_{90}	<850	90			
SAL	<850	-	S. Alfio	17/11/2013	12
SAL>850	>850	-			
SAL_{90}	<850	90			
MIL	<850	-	Milo	17/11/2013	10
MIL>850	>850	-			
MIL_{90}	<850	90			
MIL<63	<63	-			
BIA	<850	-	Biancavilla	26/10/2013	16
BIA>850	>850	-			
BIA_{90}	<850	90			
BIA<63	<63	-			
FIA	<850	-	Fiandaca	04/12/2013	15
FIA_{30}	<850	30			
FIA_{180}	<850	180			
BEL	<850	-	Belpasso	04/18/2013	18
BEL_{30}	<850	30			
$BEL<63_{90}$	<63	90			
STE	<850	-	S. Tecla	04/03/2013	20
STE_{30}	<850	30			
STE_{90}	<850	90			
STE_{180}	<850	180			
SVE	<850	-	S. Venerina	03/16/2013	14
SVE_{30}	<850	30			
SVE_{90}	<850	90			
GIA	<850	-	Giarre	02/19/2013	17
ZAF1	<850	-	Zafferana	04/20/2013	11
ZAF2	<850	-	Zafferana	04/20/2013	11
PIS	<850	-	Pisano	04/20/2013	13
ET1	500-1000	-	Catania	09/07/2011	30 km
ET2	250-500	-			
ET3	125-250	-			
ET4	63-125	-			
ET5	<63	-			
ET_{Tot}	raw	-			
MAS	<850	-	Mascali	02/19/2013	16 km
NUN	<850	-	Nunziata	02/19/2013	15 km
MAC	<850	-	Macchia	02/19/2013	16 km

*The subscript in the labels, where present, refers to the leaching time. Where not specified explicitly in the label, the granulometry is <850. ** NSEC: New South East Crater.

Table 2. Relative fractions of the reference compounds (Magnetite, Cambodianite, Olph-1a, and Fe-sulfate) used to perform LCF of the experimental sample spectra. Samples spectra that looked very similar at a visual inspection are grouped (A, B, and C). The average relative fraction of each group is reported in bold characters. Subgroups highlight smaller variations of the relative fractions. The sum of the fractions (Σ) and the chi-square value (χ^2) are also reported. The error on the calculated fractions is estimated to be ~10%. Fractions < 5% were neglected. Where not specified explicitly in the samples label, the granulometry is <850. For samples subjected to leaching, leaching time is indicated by a subscript (30, 90, or 180mn). Sample FIA_{30} (Table 1) was not measured due to the limited beamtime available.

		Magnetite %	Cambodianite %	Olph-1a %	Fe-sulfate %	Σ	$\chi^2 \cdot 10^5$
	Average	**29**	**36**	**18**	**17**	**101**	**2.6**
Group A	BEL BEL_{90} BEL<63	20	42	27	12	101	1.0
	BEL_{30}	25	38	23	16	101	2.6
	BIA>850 BIA BIA_{90}	28	37	21	15	101	2.7
	FIA FIA_{180}	21	42	26	12	101	1.0
	LIN>850 LIN LIN_{90}	30	35	17	18	101	3.3
	MIL>850 MIL MIL_{90}	39	32	13	18	101	2.2
	SAL>850 SAL SAL_{90}	34	35	13	19	101	2.4
	STE>850 STE STE_{90} STE_{180}	23	38	24	16	101	2.3
	SVE SVE_{30} SVE_{90}	35	32	15	20	101	2.0
	PIS	24	38	22	17	101	2.6
	NUN	29	35	17	20	101	1.9
	ZAF1	33	33	13	22	101	3.2
	ZAF2	25	38	21	18	101	2.6
	CIT>850	33	36	14	18	101	2.0
	GIA	31	35	20	15	101	3.9
	ET1, ET2, ET3	25	38	24	14	101	1.4
	MAC	30	33	21	16	101	2.7
	Average	**37**	**26**	**28**	**10**	**101**	**3.7**
Group B	MIL<63	34	26	29	12	101	2.0
	BIA<63	38	24	27	12	101	4.2
	ET4	46	22	23	8	101	4.1
	ET5	31	39	32	7	101	4.0
Group C	CIT CIT_{90}	54	20	-	27	101	5.2
	MAS	21	39	15	27	101	4.4

Table 3. Structural parameters obtained by shell fitting of representative samples belonging to Groups A, B, C, MAS, and of the Fe references

(Cambodianite, Magnetite, OIph1-a, and Fe-sulfate). Common Debye-Waller factors were used for the Fe-O and Fe-Fe subshells. The EXAFS amplitude reduction factor (S_0^2) was set to 0.9 all fits. The errors are estimated to be ~20% on the coordination numbers (CN), ~0.05 Å on the bond distances (R), 0.005 Å^2 on the Debye-Waller factors (σ^2), and up to 50% on the factor weighting the octahedral and tetrahedral contributions (*x,* see text). The reduced (χ_ν^2) value is also reported. [1]Giuli et al., 2011 [40]; [2]Giuli et al., 2002 [27].

		Fe-O_1	**Fe-O_2**	***x***	**Fe-Si**	**Fe-S**	**Fe-Fe_1**	**Fe-Fe_2**	**χ_ν^2**
Group A	CN	4	6				4.6	0.5	
	R(Å)	1.91	2.07	0.3			3.01	3.43	5
	σ^2(Å^2)	0.005					0.027		
Group B	CN	4	6				2.1	0.4	
	R(Å)	1.89	2.04	0.3			2.98	3.48	13
	σ^2(Å^2)	0.003					0.011		
Group C	CN	4	6			0.7	8.5	3.9	
	R(Å)	1.93	2.09	0.5		3.02	3.03	3.44	10
	σ^2(Å^2)	0.007					0.018		
MAS	CN	4	6			0.4	6.4	1.9	
	R(Å)	1.90	2.07	0.4		3.01	3.02	3.35	31
	σ^2(Å^2)	0.004				0.001	0.018		
[1]OIPh-1a	CN	4			4				
	R(Å)	1.85			3.31				
	σ^2(Å^2)	0.003			0.019				
[2]Cambodianite	CN	4.1			4				
	R(Å)	1.93	2.10		2.77				
	σ^2(Å^2)	0.002	0.010		0.007				
Magnetite	CN	4	6				3	9	
	R(Å)	1.91	2.04	0.4			2.95	3.45	33
	σ^2(Å^2)	0.008					0.009		
Fe-sulfate	CN	2	4		2		2		
	R(Å)	2.01	2.15		3.11		3.16		34
	σ^2(Å^2)	0.002			0.010		0.008		

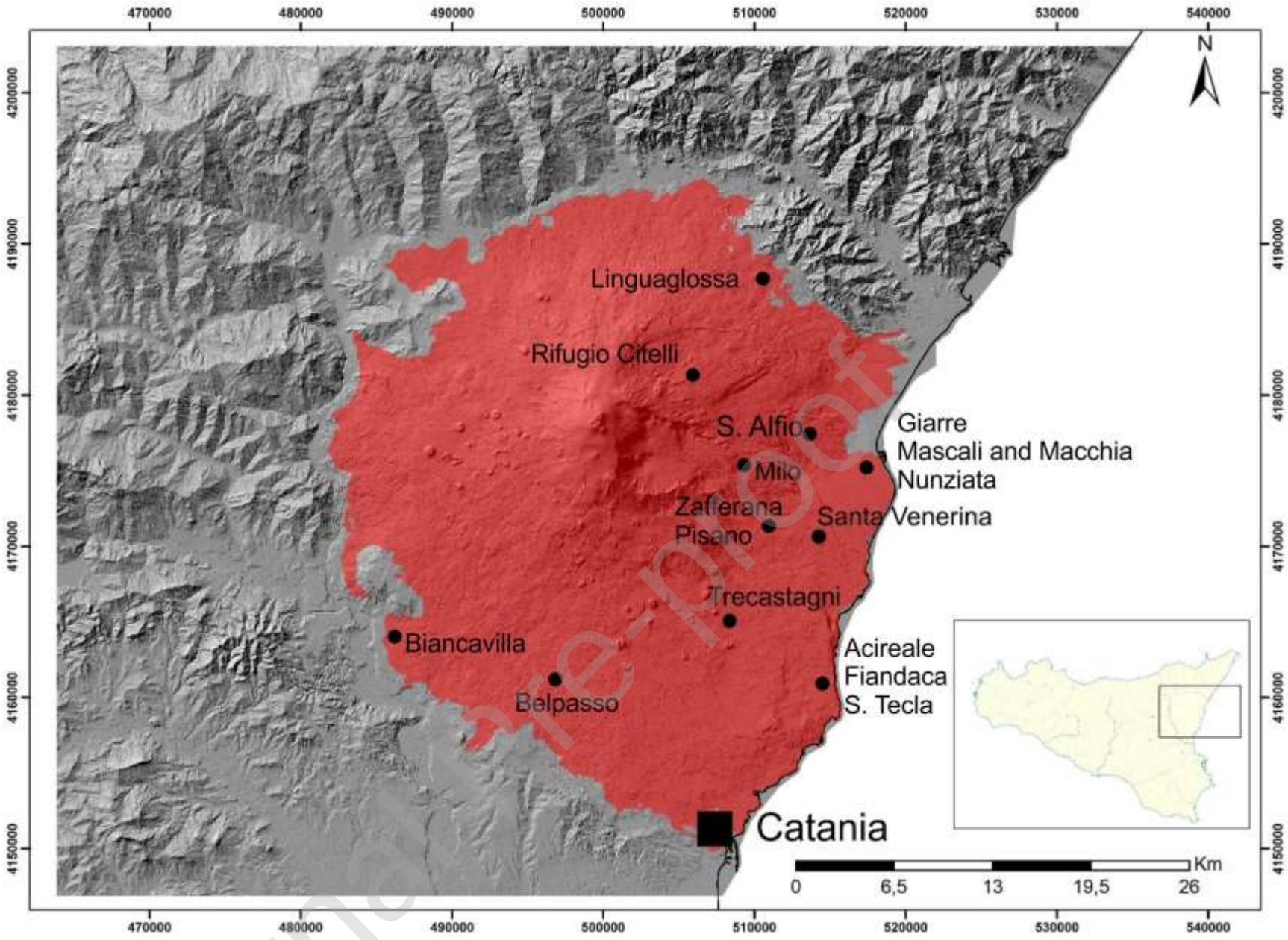

Figure 1. Map of the Mt. Etna volcanic complex in Sicily (South Italy). The localities where ashes were sampled are indicated (see Table 1).

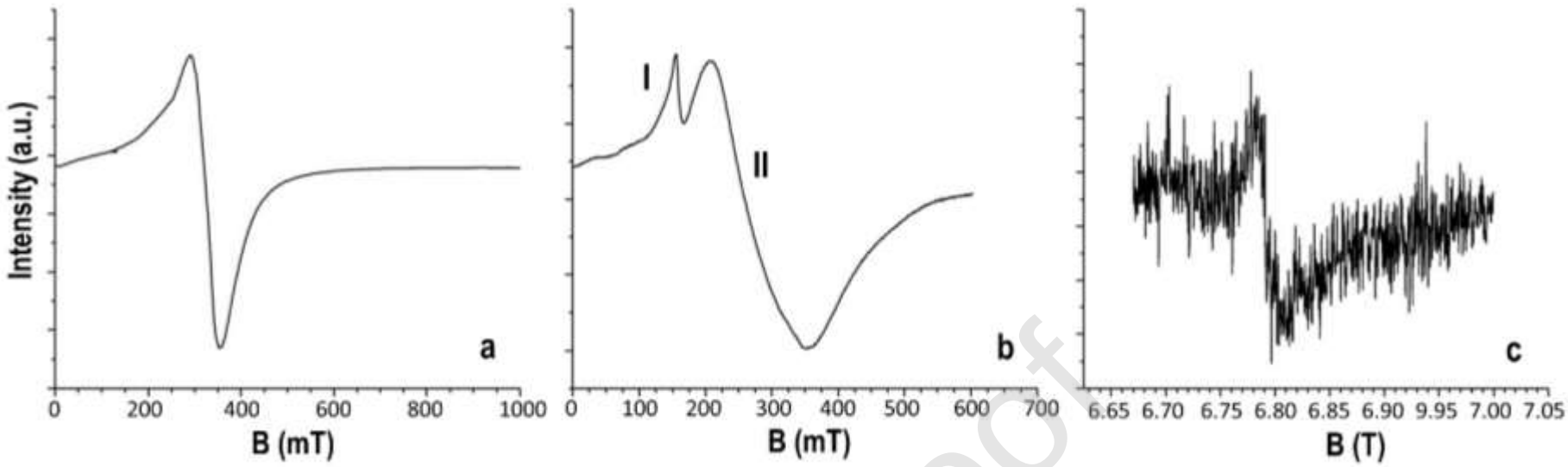

Figure 2. a) EPR spectrum of sample ET acquired at RT and at 35 K (b); c) HFEPR spectrum, acquired at 298 K and 190 GHz. The magnetic field values are expressed in milliTesla (mT) (a) and (b), and in Tesla (T) (c).

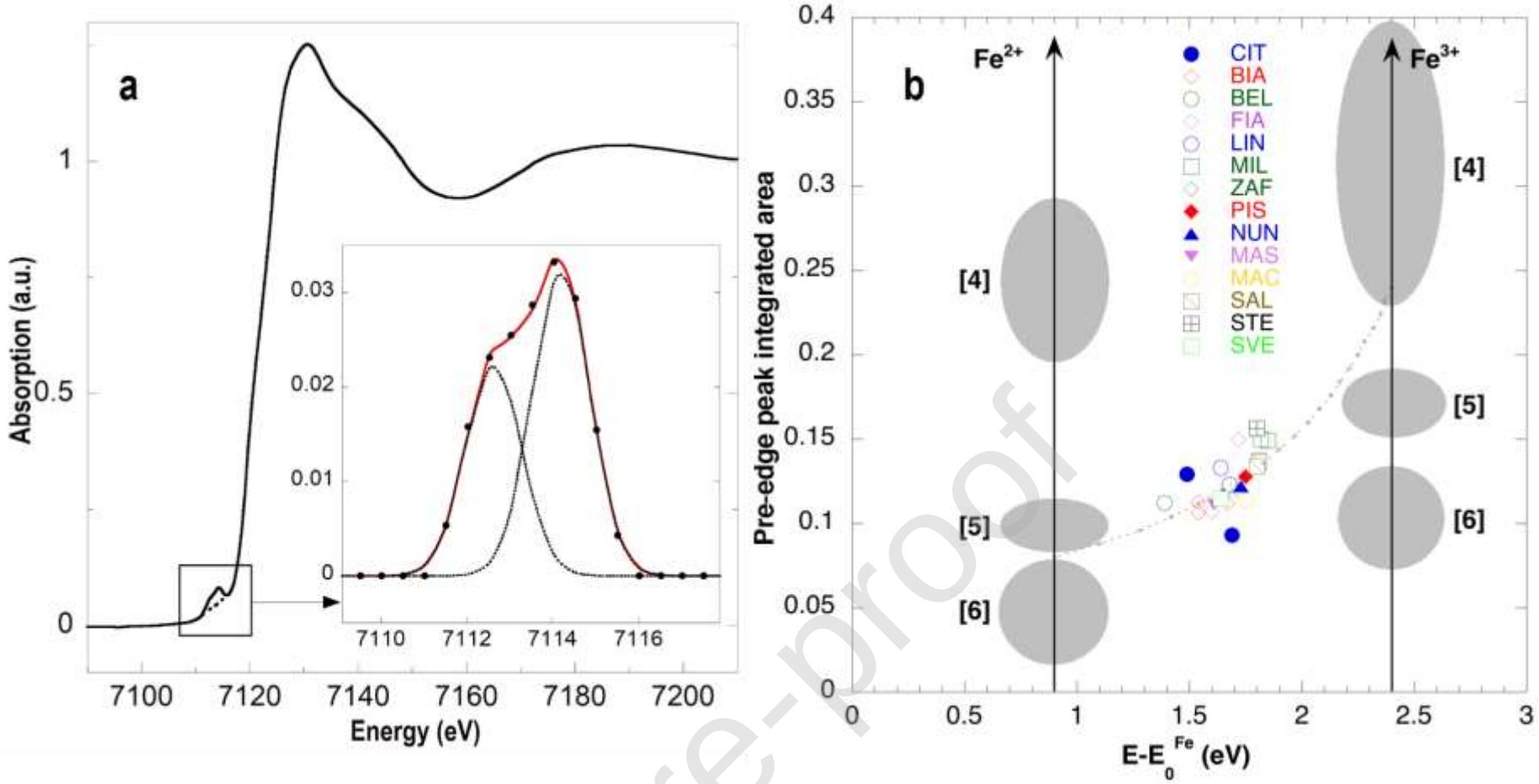

Figure 3. a) Representative Fe K-edge XANES spectrum. The inset shows the pre-edge (PE) feature (dots) obtained after the subtraction of an arctangent curve mimicking the absorption edge and the two Gaussian components used to fit the pre-edge peak (in the inset: dots = experimental data; continuous lines = best fit to the data; dashed lines = peak components). b**)** Plot of the background subtracted PE peak integrated area *vs* its centroid energy for all the samples [51], including aliquots of the same sample with different granulometry. Most of the samples can be modeled as a combination of two endmembers: i) Fe(II) with an average coordination number close to 5 (e.g. Fe(II) in the glass and/or crystalline phases), and ii) Fe(III) in tetrahedral coordination in the glass phase. The dashed curve represent the model curve obtained simulating the above combinations, and the superimposed symbols represent 0.05 steps in the Fe(III)/Fe_{tot} ratio.

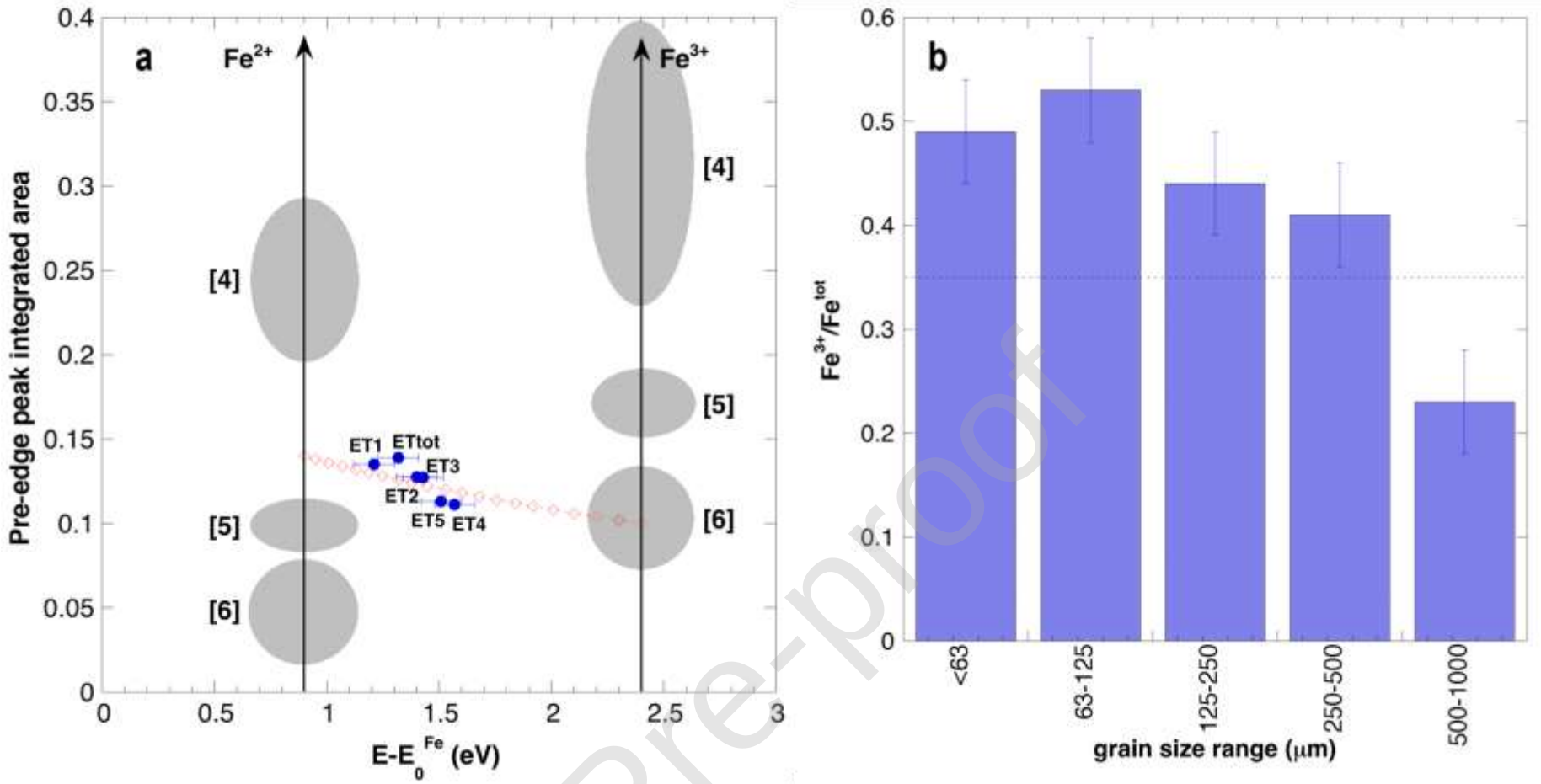

Figure 4. a) Plot of the background subtracted Pre Edge peak integrated area vs its centroid energy [51] for aliquots of the ET samples with different granulometry. The aliquots can be modeled by a combination of two endmembers: i) Fe(II) with an average coordination number intermediate between 4 and 5 (e.g. Fe(II) in the glass phase), and ii) Fe(III) in octahedral or higher coordination, representative of Fe(III) in crystalline phases. The dashed curve represent the model curve, and the superimposed diamond symbols represent 0.05 steps in the $Fe(III)/Fe_{tot}$ ratio; b) Histogram reporting the $Fe(III)/Fe_{tot}$ ratio for the ET series as a function of the samples granulometry. It is evident a decrease of the Fe oxidation state for increasing grain sizes, i.e. from ET5(<63μm) to ET1(500-1000μm).

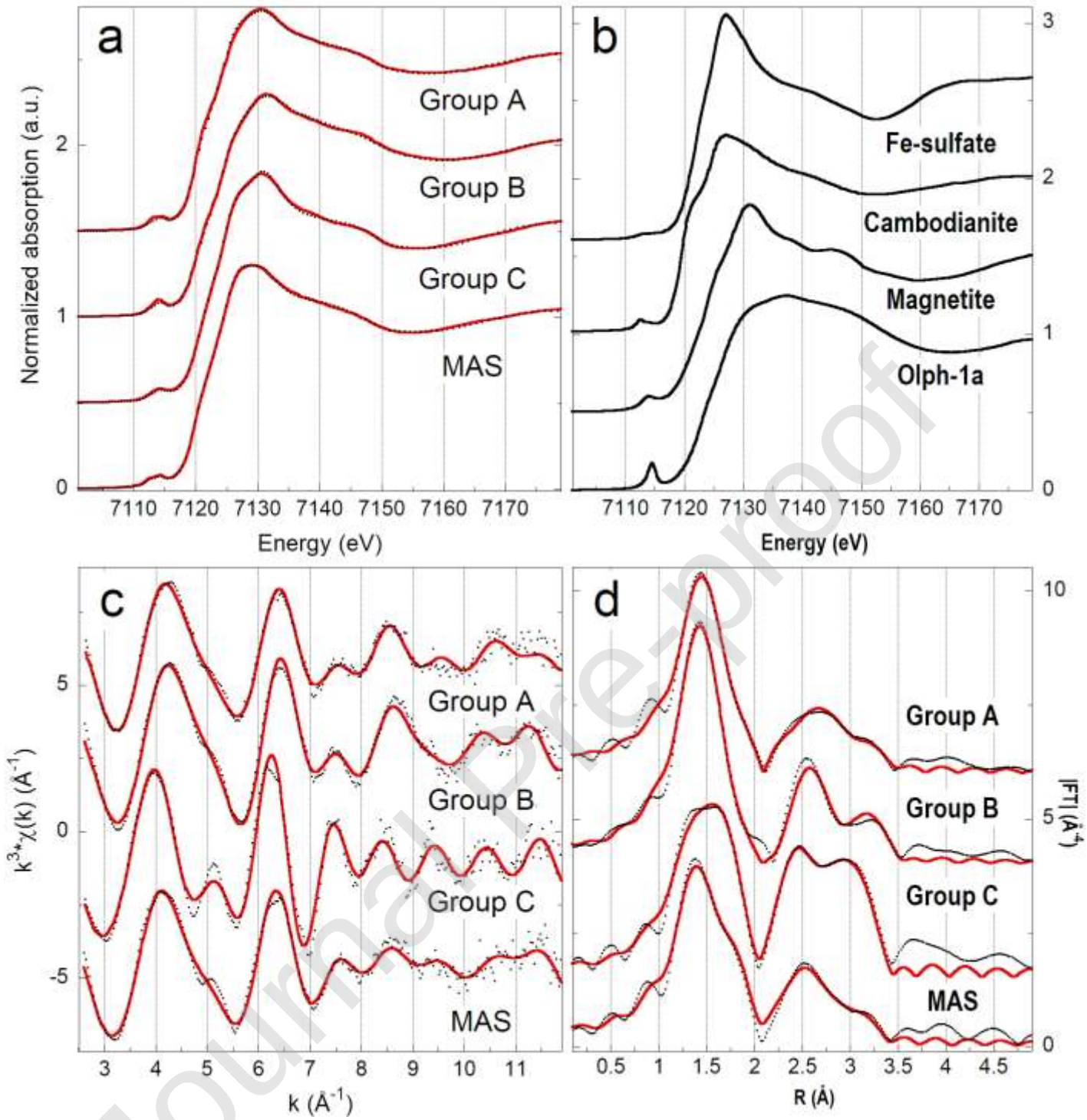

Figure 5. a) Averaged XANES spectra of samples belonging to Group A, B, and C, and of sample MAS (black dots). Solid (red) lines represent the LCF curves. b) XANES spectra of the reference compounds included in the LCF: cambodianite, magnetite, OIph-1a, and Fe-sulfate. The spectra of the other reference can be found in Figure 1 in the Supplementary Material. c) EXAFS signal of representative samples belonging to Groups A, B, C, and of sample MAS (K^3-weighted). d) Moduli of the Fourier Transforms (FT) of the EXAFS signals reported in the left panel (K^3-weighted, FT range 2.5-12 $Å^{-1}$, not corrected for the phase shift). Black dots are experimental data; solid (red) lines are the best fits.